metals

MDPI

Article

Crack Growth Patterns of Aluminum Tubular Specimens Subjected to Cyclic Tensile Loads

Lenin Abatta-Jacome [1,2,*], Luis Caminos [1], Antonio Gonzalez-Herrera [1] and Jose Manuel Garcia-Manrique [1]

[1] Department of Civil Engineering, Materials and Manufacturing, School of Engineering, University of Malaga, 29071 Málaga, Spain; lfcaminos@uma.es (L.C.); agh@uma.es (A.G.-H.); josegmo@uma.es (J.M.G.-M.)
[2] Department of Energy Sciences and Mechanics, University of the Armed Forces ESPE, Sangolquí 171103, Ecuador
* Correspondence: lrabatta@espe.edu.ec

Abstract: This study presents a detailed analysis of a fatigue test campaign in order to identify different crack patterns. It was conducted on 6061-T6 aluminum tubular specimens featuring an internal diameter of 10 mm and different thicknesses (2, 3 and 4 mm). These specimens were subjected to cyclic tensile loads with a load ratio of R = 0.1, utilizing a sinusoidal load function at a frequency of 3 Hz. The investigation examines the crack growth rates, the stress intensity factor, and the final and intermediate fracture zones by applying overloads in some cases. The differences with two-dimensional specimens and the importance of this study for the interpretation of results with biaxial loading states are highlighted. The different states of crack growth detected are analyzed using artificial vision techniques. The differences between the exterior and interior faces of the specimen are revealed, and a series of states prior to the formation of the radial crack front expected in these specimens are identified.

Keywords: fatigue crack growth; SEM; tubular specimen; cyclic tensile loads

Citation: Abatta-Jacome, L.; Caminos, L.; Gonzalez-Herrera, A.; Garcia-Manrique, J.M. Crack Growth Patterns of Aluminum Tubular Specimens Subjected to Cyclic Tensile Loads. *Metals* **2024**, *14*, 1094. https://doi.org/10.3390/met14101094

Academic Editor: Wei Li

Received: 15 August 2024
Revised: 20 September 2024
Accepted: 20 September 2024
Published: 24 September 2024

1. Introduction

Research on crack behavior subjected to fracture or fatigue processes has traditionally relied on analyzing their behavior in specimens under controlled conditions, through either experimental or numerical models. CT specimens have been widely used to simulate states of flat crack subjected to solicitations favoring mode I crack growth.

The following describes several studies and works conducted on flat specimens, with an emphasis on materials, universal testing machines, as well as numerical models, among other aspects.

For example, Jong Henk [1] analyzed fatigue crack geometry in 25-mm thick flat specimens of 7075 T651 aluminum alloy, using servo-hydraulic equipment to apply cyclic loads up to 200 kN at frequencies up to 10 Hz. Correia et al. [2] investigated the fatigue crack growth of 6082-T6 aluminum alloy per ASTM E647 standards [3], using standard CT, sharp-notched, and circular samples. They found that notch configuration significantly affects the stress intensity factor (K), with round notches yielding higher stress thresholds. CT specimens were 10 mm thick, with chevron-type notches used as stress concentrators. Loads from 2.8 to 6.2 kN extended cracks to 2 mm, requiring 14,400 to 16,600 cycles for failure. Chun-Jun [4] studied compact tension samples under 8–10 kN loads and load ratios of R = 0.1, 0.3, and 0.5, using an MTS 858 system at frequencies up to 20 Hz. Bretschneider [5] examined non-standard geometries in aluminum alloy, applying R = 0.1 load ratios until cracks reached 2.5 mm, noting similar displacement on the external faces. L. Cai [6] used optical microscopy and SEM to assess crack geometry under overloads, finding that the Paris law-based crack closure effect did not align with post-overload growth. Vasco-Olmo [7] applied digital image correlation to evaluate fatigue crack growth, proposing alternative parameters for stress intensity factors. Additionally, extensive 2D and

3D numerical modeling has been developed. Computational cost remains a critical factor in these studies. Various models have analyzed crack edge behavior, focusing on plastic deformation and stress [8–15]. Camas et al. [16] demonstrated that plastic deformation is more pronounced near the external faces of flat specimens, with similar deformation observed on both faces.

Having thoroughly reviewed the extensive research on flat specimens, attention is now directed towards investigating studies conducted on tubular specimens.

Tanaka [17] performed fatigue crack growth tests using thin-walled tubular specimens with a circular hole made of low-carbon steel. Cyclic uniaxial compression, tensile loads, and cyclic torsion were applied. Crack growth rates for torsion and torsion, combined with axial loading, were higher than uniaxial loading. The crack growth acceleration was attributed to increased plasticity at the crack tip. Shamsaei [18] conducted research involving strain-controlled tests on tubular specimens made from pure titanium and titanium alloy BT9. The study included both constant and variable amplitude axial and torsional loads, as well as in-phase and out-of-phase axial-torsional loading conditions. Gladskyi [19] investigated the effects of notches on the fatigue behavior under axial and torsional loading in thin-walled tubular specimens of low-carbon steel. He evaluated specimens with and without a transverse circular hole. It was determined that the notch effect was more pronounced under axial loading. Fatemi [20] conducted fatigue tests of thin-walled 7075-T6 and 2024-T3 aluminum tubular specimens with a circular notch. The loading conditions applied were torsional and axial ones. Macroscopic crack growth in notched specimens occurred along planes experiencing the maximum range of nominal principal stress, i.e., mode I crack growth; crack growth was performed by evaluating the growth on the external face associated with the external radius. Gladskyi [21] evaluated the fatigue crack growth of tubular specimens with a circular through-hole in carbon steel specimens subjected to axial and torsional loads, observed mode I crack growth, and the crack growth rates were correlated with the stress intensity factor, and graphs of da/dn versus K_I were generated to investigate the crack growth behavior of tubular specimens. Mokhtarishirazabad [22] carried out research related to tubular specimens, where he focused his research on the analysis of crack displacement by DIC; this research was based on the growth of the visible crack, the outer one, and the crack growth variables correlated with the stress concentration factor. Macek [23,24] investigated the fracture surface topographies of tubular specimens using an optical measurement system. It was established that these topographies are a critical factor affecting the service life of the specimens.

Regarding the numerical models of tubular specimens, numerous investigations have been conducted on this subject [25–27]. However, the conclusions of these studies consistently reveal three-dimensional crack behavior in the region near the crack, where the curvature of the crack is influenced by the distribution of the stress intensity factor (K_I) through the thickness and the phenomenon of crack closure [27]. The conclusions validated the methodology, and interesting study parameters regarding crack growth rates between the outer and inner faces of the specimen under mode I fatigue were established. Building upon the previous results, an experimental campaign is proposed on tubular specimens under mode I solicitations, the results of which are presented in this paper.

As mentioned before, previous work focusing on fracture numerical models of tubular specimens under mode I has been conducted [27]. The analysis of the results obtained from the plastic zones was influenced by the thickness, the level of applied load, and by the radius of curvature. The work presented in this article is proposed as a continuation of the previous one and presents a fatigue-testing campaign of different specimens of aluminum tubular specimens subjected to tensile loads. The internal radius has been kept constant and the crack is evaluated in three cases with different thicknesses, focusing on the evolution of the crack on the outside. The relationship with the analytical values of the stress intensity factor (both internally and externally) is analyzed.

This article is structured as follows: A brief description and justification of the methodology used. Next, the results obtained are presented, followed by an extensive analysis of the results, and finally the research conclusions are described.

2. Materials and Methods

This section addresses the technical parameters of the experimental part. Three tubular specimens of different thicknesses made of 6061-T6 aluminum (Yield strength 276 MPa, Ultimate tensile strength 310 MPa) [28], a material widely used in the industry in structural applications, fluid conduction and machine components, are studied.

2.1. Geometry

This research analyzes three tubular specimens with a constant internal diameter of 10 mm, a central one with 3 mm of wall thickness, and two additional cases of smaller and larger thickness—2 and 4 mm thickness, respectively. A cylindrical bar of 38 mm in diameter was used to construct the specimens. It was subsequently machined with conventional manufacturing processes, i.e., turning, milling, and drilling until reaching the desired geometry (Figure 1). Perpendicular to the longitudinal axis of the specimen, a cylindrical notch-type stress concentrator of 1.5 mm in diameter was located in the center of the specimen, the place where the crack will initiate, the latter having been previously calculated by applying material resistance techniques.

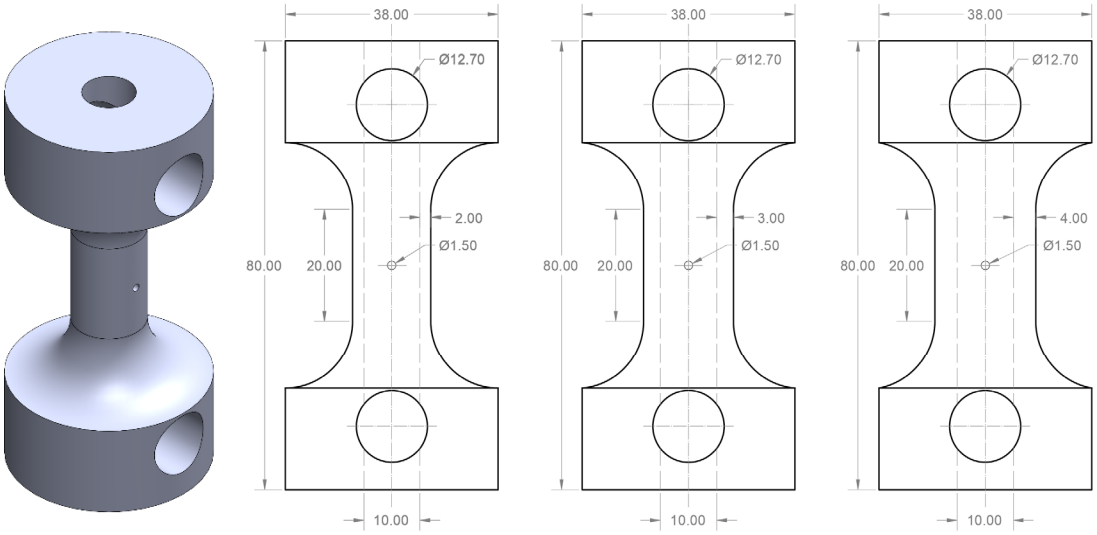

Figure 1. The geometry of 6061-T6 aluminum tubular specimens. Units in mm.

The specimen with a wall thickness of 3 mm was carried out from nucleation (from an initial stress concentrator) to failure with a constant cyclic load value. The evolution of the exterior crack was recorded, and the K_I value on the exterior was calculated. Only the final mark at the beginning of the complete fracture is available to interpret the shape of the crack. In the cases of 2 and 4 mm, it was decided to apply an overload in the middle part of the experiment, which allowed us to identify the shape of the crack at that point, although slightly altering its development. The load values were chosen to be at an intermediate value with respect to the fracture value, as seen in Section 2.3.

2.2. Stress Intensity Factor

The stress intensity factor was calculated both on the outside and inside of the tubular specimen. The proposal of Sanders [29], who derived the solution for a circumferential

energy release rate through a crack extending in a cylindrical shell subjected to axial tension, was used. The energy release rate (concerning crack angle) is:

$$I = \frac{\partial}{\partial a} \int_{-\pi}^{\pi} u_c d\theta \tag{1}$$

where u_c is the dimensionless displacement, and a corresponds to the crack growth in the axial direction. Forman [30], based on the proposal of Sanders [29], defines the following Equations (2)–(12) for the calculation of stress intensity in tubular specimens subjected to tension:

$$K_I = F_0 \, \sigma_1 \, \sqrt{\pi a} \tag{2}$$

where:

$$a = \alpha * R \tag{3}$$

$$F_0 = \sqrt{\frac{I_0}{2 \, \pi \, \alpha}} \tag{4}$$

$$I_0 = \left[\sqrt{8} \left(f^2 - 1 \right) + \frac{\pi \, \beta^2}{b} \right] \frac{\alpha^2}{k} \tag{5}$$

$$f = 1 + \frac{h \, (1 - \alpha \, cot\alpha)}{2\alpha} \tag{6}$$

$$\beta = 1 + \left(\frac{\pi}{16} \right) b^2 - 0.0293 \, b^3 \text{ for } b \leq 1 \tag{7}$$

$$\beta = \left(\frac{\sqrt{8b}}{\pi} \right)^{0.5} + \left(\frac{0.179}{b} \right)^{0.885} \text{for } b > 1 \tag{8}$$

$$b = \frac{\alpha}{2k} \tag{9}$$

$$k = \sqrt{\frac{t}{R}} \left[12 \left(1 - v^2 \right) \right]^{-\frac{1}{4}} \tag{10}$$

$$h = \frac{\sqrt{2}}{\left\{ cot \left[\frac{(\pi - \alpha)}{\sqrt{2}} \right] + \sqrt{2} \cot \alpha \right\}} \tag{11}$$

$$2a = 1.5 + 2 \, c \tag{12}$$

The parameters a, R, and c are geometric characteristics of the tubular specimen (see Figure 2), units in millimeters; I_0 is the dimensionless energy release rate integrals; σ_1 is the remote tension stress; and v is Poisson's ratio.

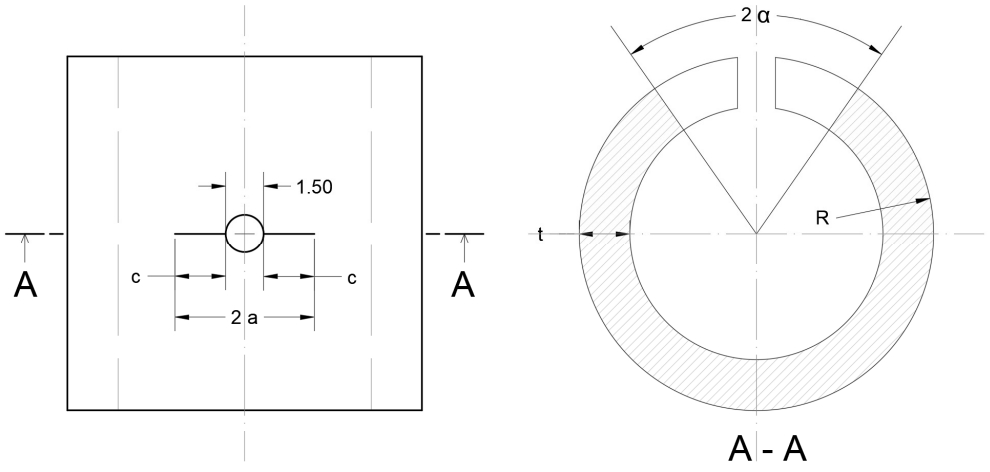

Figure 2. Geometric considerations for calculating the stress intensity factor, units in millimeters.

2.3. Definition of Load and K_I Parameters for the Experimental Test

As a prior step to applying cyclic loads, static tensile destructive mechanical tests were carried out with monotonic loads for the three thicknesses studied (Figure 3).

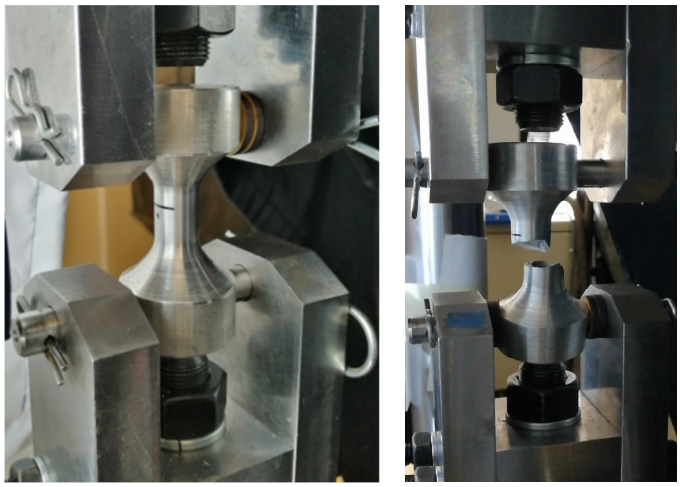

Figure 3. Tensile test, monotonic loading, and failure verification through the stress concentrator.

Figure 4 shows the results of the tensile test for a tubular specimen with a 2-mm wall thickness, displaying the applied load and the K_I value calculated on the specimen's exterior according to expression 2 of Section 2.2. To know the K_I values applicable before the crack growth in the circular stress concentrator, experimentally, no crack growth was shown until the maximum load P, where the load-bearing capacity of the specimen was exhausted. After maximum loading, the specimen fractured abruptly at the stress concentrator.

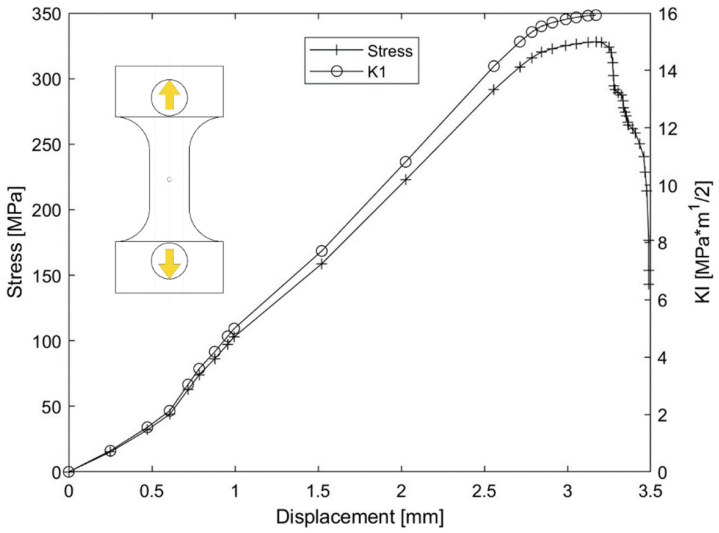

Figure 4. Static mechanical test of a tubular specimen with a wall thickness of 2 mm.

The stress intensity factor increased its value with crack growth when cyclic loads were applied to the specimen, producing fatigue. For aluminum alloys, the K_I value could be between 20 and 40 MPa $m^{1/2}$. It was determined that the value of the maximum stress intensity factor obtained through a static tensile test, without crack growth, was 16 MPa $m^{1/2}$ (Figure 4). However, the theoretical value was relative to the exterior, for reference throughout the article.

As detailed later, the distribution of K_I was not constant in thickness. Although we cannot know what this distribution is like, we can understand that K_I had a greater value

on the inside since the crack was longer than on the outside. Regarding the fracture values, referring to the theoretical value relative to the exterior, the maximum fatigue load values were chosen to be at an intermediate value for the fracture value around K_I = 8 MPa m$^{1/2}$. In the case of the specimen with a wall thickness of 4 mm, it was observed that it was impossible to advance the crack at these values, so it was increased to a value prior to breakage.

Previous work on flat specimens [2,4,5,31] used different fatigue testing systems, including the Instron 8801 equipment (Norwood, MA, USA) used in this research, to produce fatigue at constant load, therefore, the K_I values grew with the crack. The equipment was configured with the following parameters: cyclic loads, load control, load application frequency of 3 Hz, sinusoidal load shape function, and load ratio R = 0.1. Table 1 summarizes the parameters applied in the initial condition:

Table 1. Loading conditions applied to tubular specimens.

Wall Thickness [mm]	Loading Frequency [Hz]	Load Function	Maximum Initial K_I Re MPa m$^{1/2}$	Minimum Initial K_I Re MPa m$^{1/2}$	Maximum Load [N]	Minimum Load [N]
2	3	Sinusoidal	7.9456	0.79456	11,770.0	1177.2
3	3	Sinusoidal	8.5064	0.85064	20,600.0	2060.1
4	3	Sinusoidal	15.9591	1.59591	55,720.0	5572.08

These parameters were selected without exceeding the maximum stress intensity value obtained through the static destructive mechanical test. In order to characterize the geometry of the crack, an overload was applied to the 2- and 4-mm specimens, similar to previous work [6]. Subsequently, the application of cyclic loads continued until the total failure of the tubular specimens.

For comparative purposes, exclusively cyclic loads were applied to the specimen with a wall thickness of 3 mm until failure, without applying a crack marking load. The fracture zone was analyzed through electron microscopy techniques. The equipment used was a TESCAN MIRA 3 scanning electron microscope (Brno, Czech Republic). The images obtained by the microscope were digitally post-processed for later comparison with previous works.

3. Results and Discussion

This section presents the results obtained, emphasizing the fracture zone. Crack growth was estimated, and the fracture zone after applying cyclic loads was evaluated by relating its behavior to the external radius Re and the internal radius Ri (Figure 5).

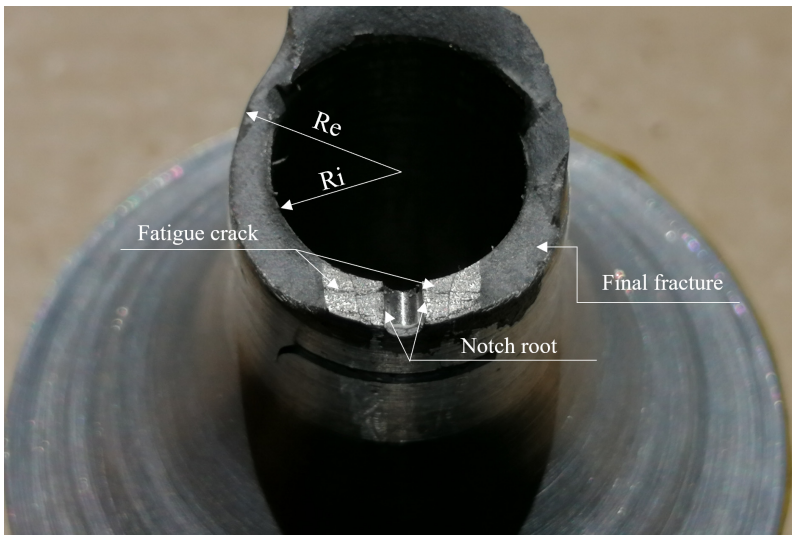

Figure 5. The fracture zone in the stress concentrator is a specimen with 2 mm of wall thickness.

3.1. Analysis of Stress Intensity Factor

Once the initial K_I parameters to be applied to the specimens were defined, Table 1 calculated the variation of the stress intensity factor as a function of the crack growth associated with the internal and external radii. The formulation proposed by Forman [30] was used (Equation (2)).

In Figure 6, the variation of the parameter F_0 as a function of the progress of crack growth was evaluated. It was found that this factor increases directly proportionally to crack growth. Also, variations in F_0 are observed between the interior and exterior as the crack grows. Figures 6 and 7 present the normalized crack growth on the x–axis, with respect to the thickness of the specimen.

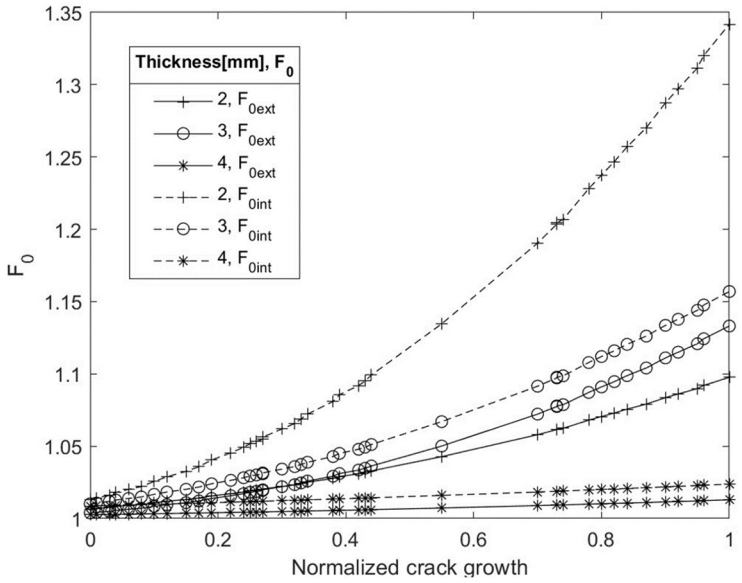

Figure 6. Variation of the F_0 factor concerning crack growth.

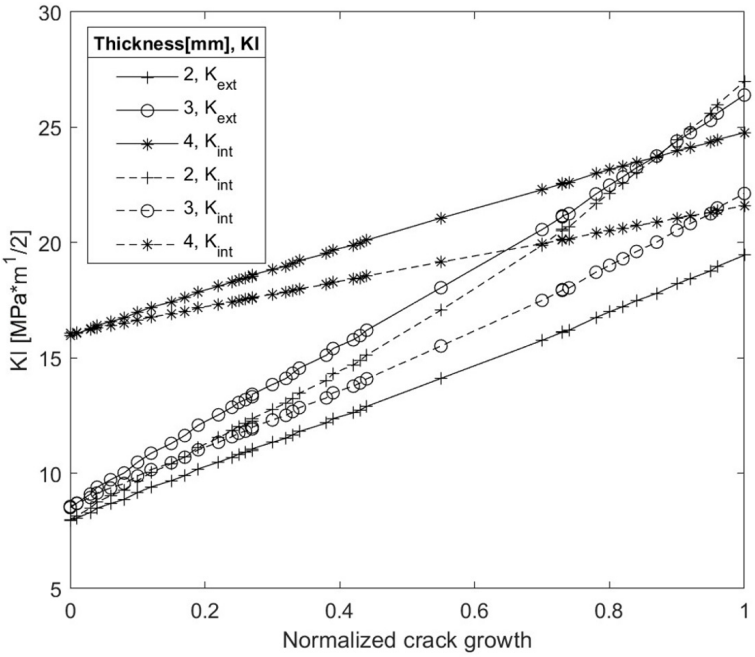

Figure 7. Variation of the stress intensity factor concerning crack advancement.

Analyzing its variation concerning thickness, it was found that the F_0 factor was inversely proportional to the thickness of the specimen, that is, with a lower thickness the

F_0 coefficient was greater. Specifically, it was observed that in the specimen with 2 mm of wall thickness, the differences were negligible at the beginning and very large as the crack grew, while, at the other end of the specimen with 4 mm of wall thickness, the variation was greatly reduced. For this reason, the 3 mm specimen was chosen as a reference for this study as it is an intermediate case. When relating the presented values of F_0 concerning the faces associated with the internal and external radii, it was found that this factor was higher in the internal radius than the external radius.

Figure 7 analyzes the stress intensity factor K_I for crack growth. It was observed that K_I increases its value directly proportionally to the crack size. Also, it was identified that the stress intensity factor had different values from the faces associated with the internal and external radii, a characteristic of tubular specimens. The analyzed specimens of 2, 3, and 4 mm of wall thickness showed their final exhaustion when the component reached an average stress intensity factor of 26.04 MPa $m^{1/2}$.

The maximum value of stress intensity factor at which the specimens failed was associated with the internal radius for the specimen with 2 mm of wall thickness with a value of 26.98 MPa $m^{1/2}$. In comparison, 3- and 4-mm-thick specimens were presented in the external radius with values of 26.39 MPa $m^{1/2}$ and 24.76 MPa $m^{1/2}$, respectively. This variation in the location of the maximum value of the stress intensity factor was due to the manufacturing processes of the specimens. However, upon reaching the average maximum value of the stress intensity factor of 26.04 MPa $m^{1/2}$ whether it was on the face associated with the internal or external radius, the tubular specimen exhausted its capacity to withstand cyclic loads.

3.2. Global Analysis of the Fracture Zone

The crack propagation region developed adjacent to the 1.5-mm diameter circular stress concentrator. The crack propagation region of the tubular specimens after failure was analyzed. In this region, cleavage rivers were evident, a typical feature of aluminum when subjected to cyclic loads that induce fatigue.

Post-processing was carried out on the images obtained from the microscope. Engineering software (MATLAB R2023a) was used for the analysis to maintain the scale by generating the specimen's geometry. The circular notch, stress concentrator perforation, fatigue fracture zone, and final fracture zone were identified. The geometry of the crack corresponding to overload is graphed in blue, and the final fracture is graphed in red. Geometric differences in the shape of the crack were identified in the three thicknesses of specimens analyzed. The geometry of the crack due to overloading shows similar morphological characteristics to that produced by the final fracture.

In Figure 8, the specimen with a wall thickness of 2 mm is observed: The final crack and the overload crack indicate that the interior grew faster than the exterior. The initial K_I value of the exterior rapidly increased as the crack grew inside. The pattern appears stable since overload. It does not appear that it can be associated with a straight crack topology.

Figure 9 shows a tubular specimen with a wall thickness of 3 mm. The end mark is evaluated, and a radial crack is observed, with a slight curvature probably caused by the crack closure on the interior and the redistribution of load (increase in K_I in the center [32]). It is the specimen that represents normal behavior, similar to CT cracks, and will be analyzed in detail in Section 3.4.

In Figure 10, the fracture zone of the tubular specimen with a 4-mm wall thickness is shown. In this case, the thickness appeared to be so wide that the crack took too long to develop. A larger load must be applied (relative to K_I on the outside). When the overload had not yet started, it resembled a 3D lenticular crack rather than a straight crack. It broke early (due to the highest load level) when the crack appeared to begin to form.

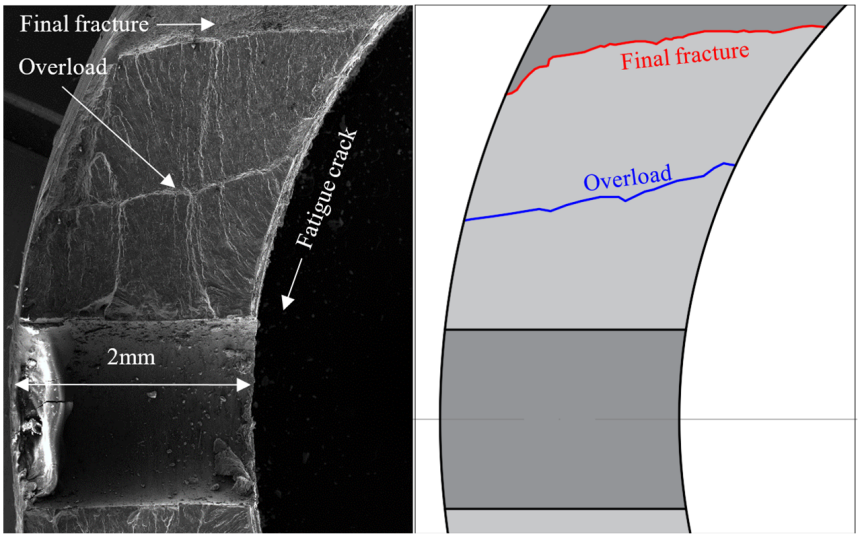

Figure 8. Fracture zone specimen with 2 mm wall thickness; blue overload crack, red final fracture.

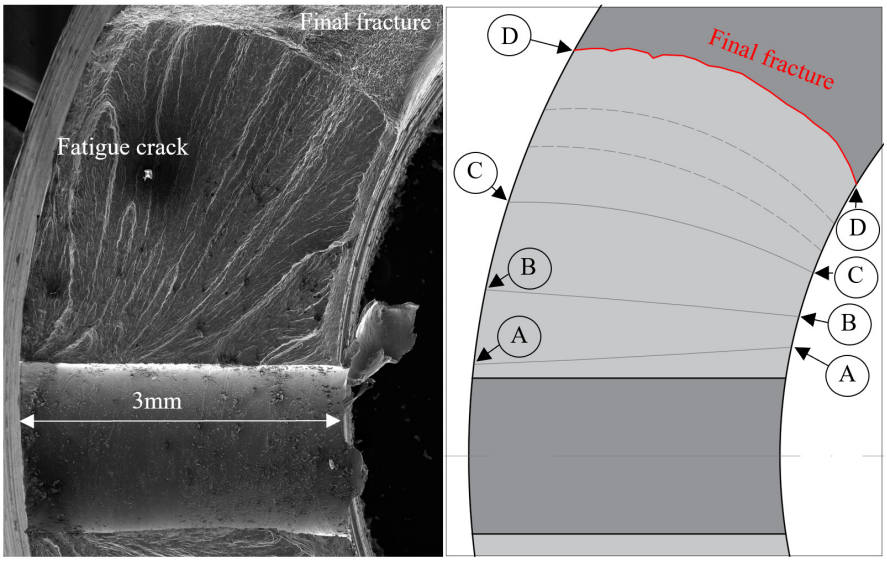

Figure 9. The fracture zone of a specimen with 3 mm wall thickness.

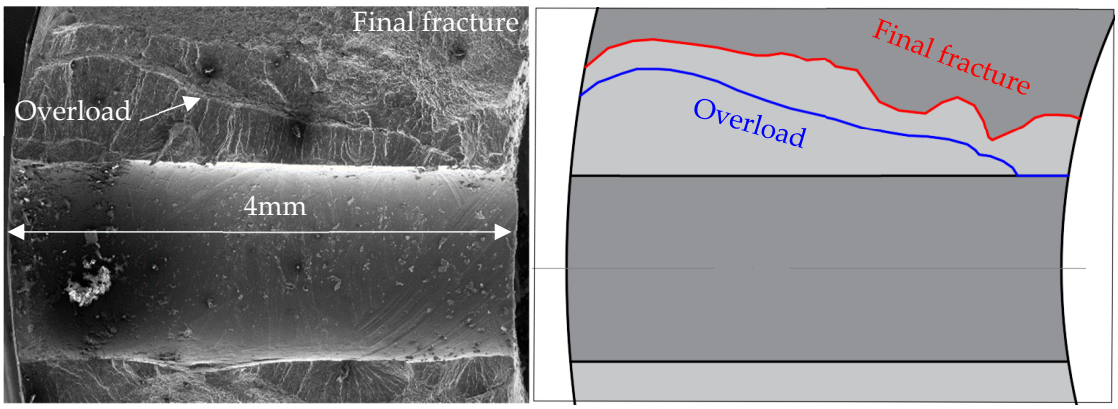

Figure 10. Fracture zone of the tubular specimen with a wall thickness of 4 mm; the blue line indicates the marking of an overload-induced crack, while the red line indicates the final fracture.

3.3. Analysis of Crack Growth

In this section, the arc length corresponding to the crack displacement on the external faces of the specimen, relating to Re and Ri, was evaluated. The length was measured from the notch, perforation of the stress concentrator, to the overload, and, finally, to the final fracture of the tubular specimen. As for the 2-mm-thick specimen, it is shown that the displacement length of the crack due to overload had a value of 0.92 mm associated with Re, and 1.44 associated with Ri. The corresponding displacement length of Ri was 1.56 times greater than that of Re. When evaluating the same parameter related to the crack formed by the final fracture, shown in red, a ratio of 1.39 was found. Therefore, a slight global variation is shown in the inclination of the crack with overload and the final fracture, being a particular case of tubular specimens compared to flat specimens, which present a similar crack displacement on the external faces of the specimens [31] (Figure 11).

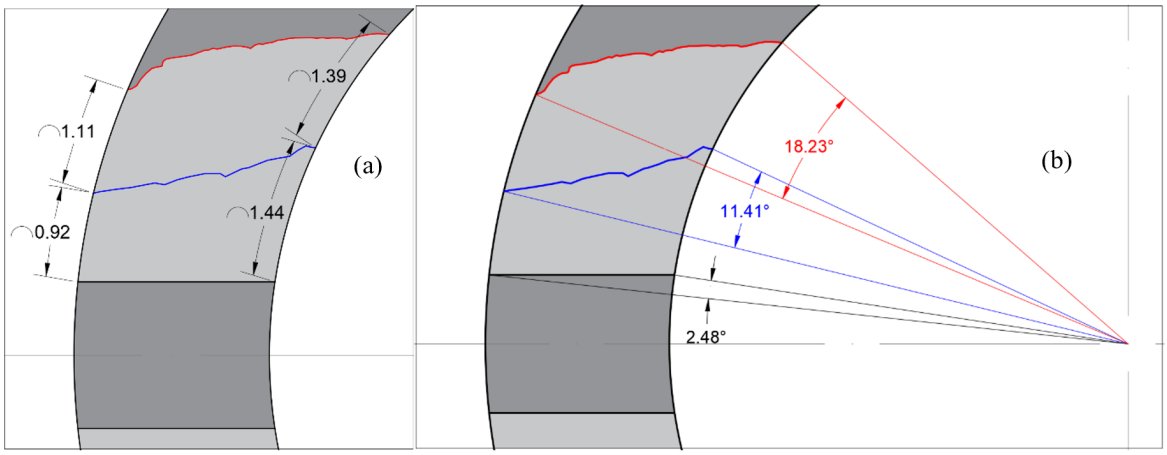

Figure 11. Specimen 2 mm thickness. (**a**) Arc length at the crack end associated with Re and Ri. (**b**) Angles generated in the notch and the crack.

Another important parameter that was evaluated is the angle formed at the two ends of the crack, concerning the origin of co-ordinates of the tubular specimen, the axial axis. It was found that, for the specimen with a 2-mm wall thickness, the angle of the initial plane had a value of 2.48° corresponding to the perforation of the stress concentrator notch. The angle generated at the ends of the overload crack was 11.41°. Finally, the crack angle associated with the final fracture was 18.23°. When relating these angles, it was found that the angle of the final fracture concerning the overload was 1.59 times greater. It was also identified that the initial angle varied as the crack moved.

In order to evaluate and relate the parameters associated with Re and Ri, the area of the fracture zone was calculated, differentiating the overload and the final fracture. Areas associated with Re and Ri are considered to calculate the areas. Half the thickness was identified from the external face to a median-curved plane associated with Re, and from the median-curved plane to the internal face associated with Ri. It was found that, until overload, the area associated with Ri was greater by 1.23 times than the area associated with Re. When evaluating the areas generated until the final fracture, it was evident that the area associated with Ri was 1.12 times greater than that associated with Re (Figure 12).

Table 2 shows a global summary of the results. A clear difference is identified between the data obtained with Re and Ri. The variation in the different parameters may be related to the plastic deformation responsible for crack closure; it was found that, at the crack tip, there were different values in the two associated crack ends, Re and Ri. On the other hand, this variation in results may also be because the normal stress at the crack tip was not the same along the crack, varying at the ends close to the walls of the specimen, being different values when associated with Re and Ri.

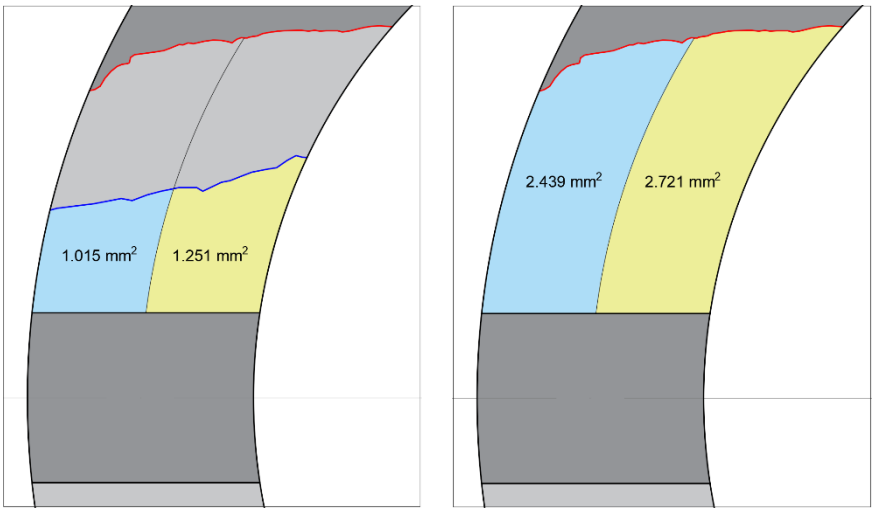

Figure 12. Specimen of 2 mm thickness, left until overload, right until final fracture, fracture areas associated with Re and Ri.

Table 2. Global summary of results of the final fracture zone, specimens of 2, 3, and 4 mm of wall thickness.

Wall Thickness [mm]	Number of Cycles	Arc Length Re [mm]	Arc Length Ri [mm]	Fracture Zone Area Re [mm²]	Fracture Zone Area Ri [mm²]	The Angle between the Start and End of the Crack
2	3664.0	2.03	2.83	2.439	2.721	18.23
3	7025.0	3.33	2.00	4.954	3.999	2.34
4	3968.0	0.89	0.47	2.062	1.120	3.62

3.4. Analysis of Crack Growth in the 3-mm Wall Thickness Specimen

The crack growth associated with the external face of the specimen with a 3-mm wall thickness was evaluated through artificial vision techniques. Figure 13 shows the progression of the crack on the exterior due to the application of cyclic loads. On the right *y*–axis, K was calculated relative to the external crack, and followed a proportionality with respect to it (as expected from Equation (2)). It should be noted that, depending on the progress inside the crack front, the global K does not have to follow this proportionality.

Figure 14 shows the growth rate and evolution of the crack as a function of the value of K on the outside. The pattern observed in this curve is quite anomalous compared to flat CT-type specimens [33]. This oscillatory behavior is due to the fact that crack growth is different on the inside compared to the outside of the tubular specimen [21], also affected by manufacturing processes that may have created stress concentrators on either the internal or external surface of the specimen. This characteristic does not occur in flat specimens, which exhibit uniform crack growth on the external faces [34]. To explain it, we must interpret what is happening inside the specimen.

A group of critical points (A, B, C, and D) have been marked that delimit four stages of crack growth on the outside of the specimen (I, II, III, and IV). In stage I, no growth is observed. From (A), the growth of the crack begins on the outside and advances rapidly during stage II. In (B), the growth rate is reduced and a stage of sustained growth begins (III). In the last stage (IV), the growth rate accelerates again until breakage in (D). These critical points are included in Figure 10. It is important to highlight that these are hypotheses based on data obtained in the exterior face and from the initial and final crack shapes. The experiment does not allow us to know what is happening inside the specimen. Future numerical analysis is needed to be more accurate about intermediate crack shapes.

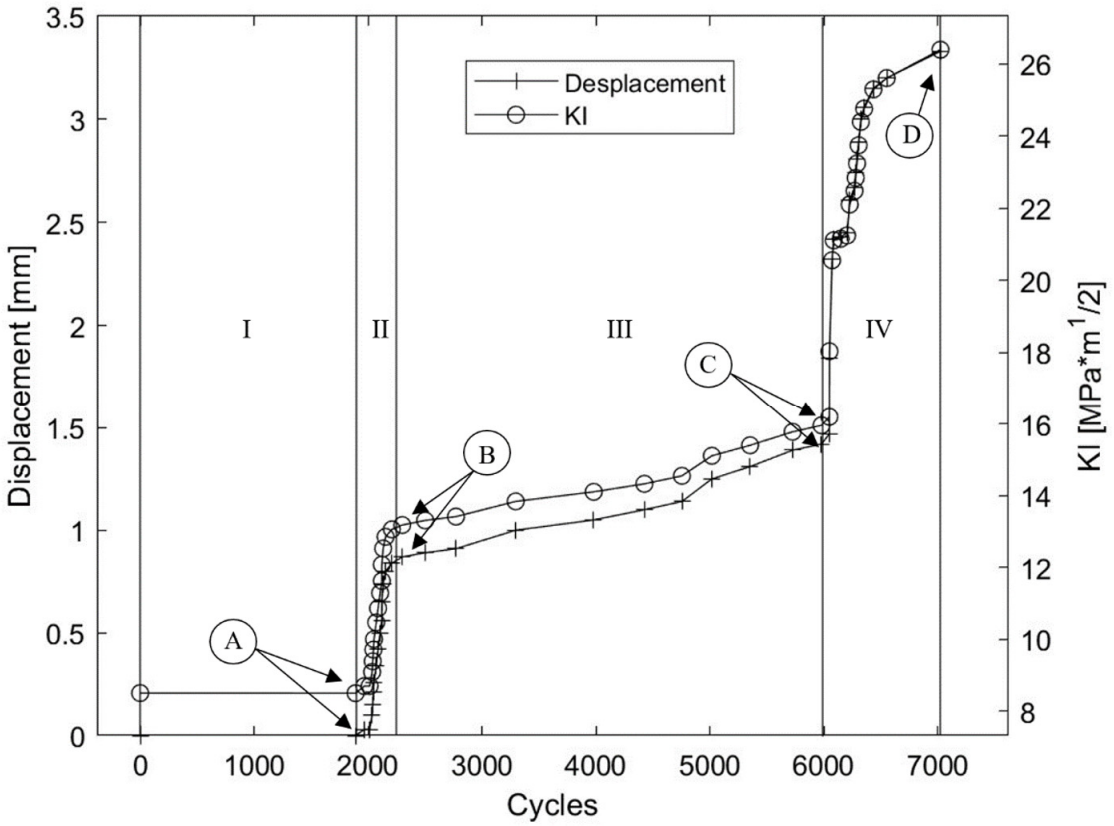

Figure 13. Crack growth associated with the external face of the specimen with a 3 mm thickness.

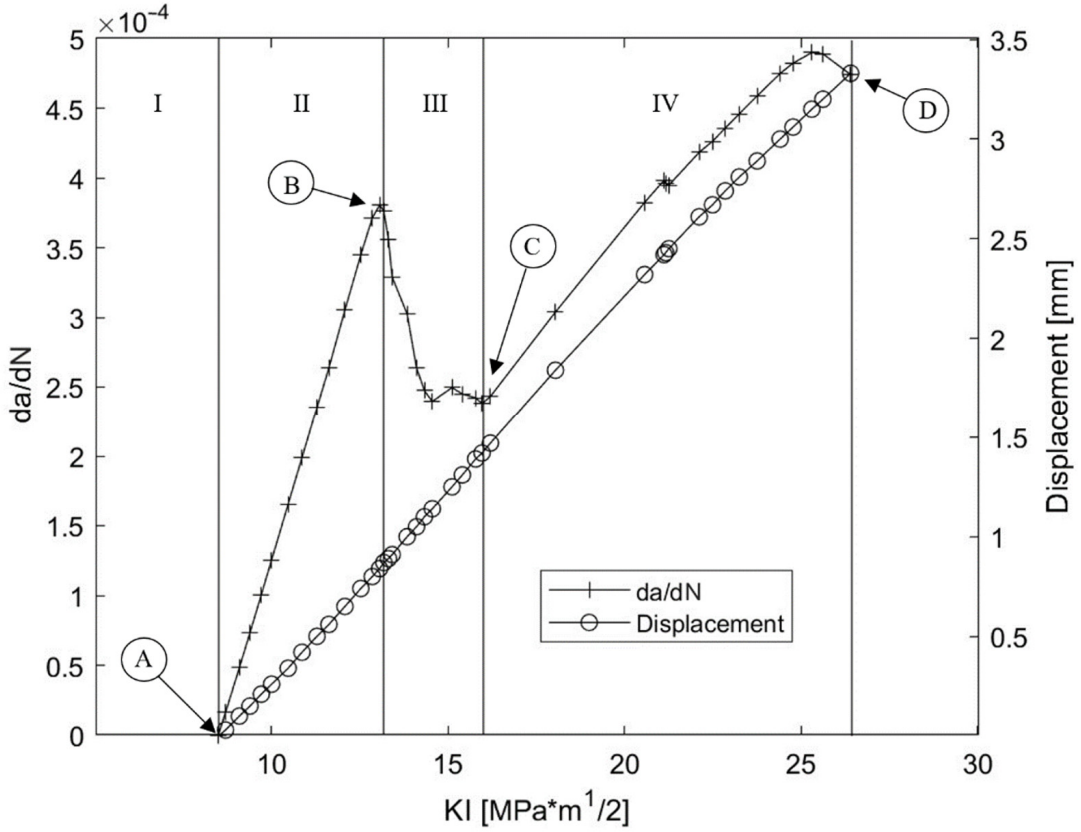

Figure 14. Relationship between crack growth rate and stress intensity factor range. Specimen with a 3 mm thickness.

The initial shape of the crack, being a straight and not conical hole, implies that, on the inside, the crack was circumferentially larger than on the outside, implying a higher K value than on the outside and, therefore, greater growth. Therefore, it would explain why, in the first 2000 cycles, no crack growth was observed on the outside. During stage I, the crack would grow with a pattern similar to that marked in Figure 10 and similar to that observed in the 2 mm specimen throughout the growth process.

Once the exterior, K reached a value similar to the other face beginning to grow, and it probably did so faster in stage II. It can be observed in Figure 9 that the length traveled on the exterior face of the specimen between points B–C and C–D was greater than that traveled on the interior face. There is a point (C) where this speed increased considerably until breakage occurred.

In state IV, a proportional relationship was reached between the speed of crack growth and the value of K, which was expected in a growth of this type of specimen. Where the crack advanced, its length increased and the analytical value of K was based on the same. From this point (C) we can assume that we already have a radial crack shape whose global K will respond in a similar way to the K calculated based on the external length.

If this point is confirmed in subsequent studies, it is very relevant because it indicates that, until this state IV occurs, the crack front in the tubular specimen does not correspond to the radial front that is sought to simulate three-dimensional fatigue states in the experiments.

3.5. Comparative Analysis of Final Fracture Zones

Another interesting point of analysis is to compare the shape of the crack when the specimen fractures between the different thicknesses of 2, 3, and 4 mm. For this purpose, the thickness was divided every 0.05 mm with parallel circumferences. The arc length of each division was calculated from the stress concentrator's notch perforation to intersect with the crack under analysis to normalize and compare results. Figure 15 shows normalized data of the fracture zone for 2, 3, and 4 mm thicknesses, and the data trend line is added. A similar trend in crack shape was found in the 3- and 4-mm-thick probes. The shape of the final fracture of the three specimens shows a characteristic difference compared to flat specimens since these, in their central part, show a data trend line with a slope similar to zero [5]. In contrast, the tubular specimens have a slope different from zero, associated with Re and Ri.

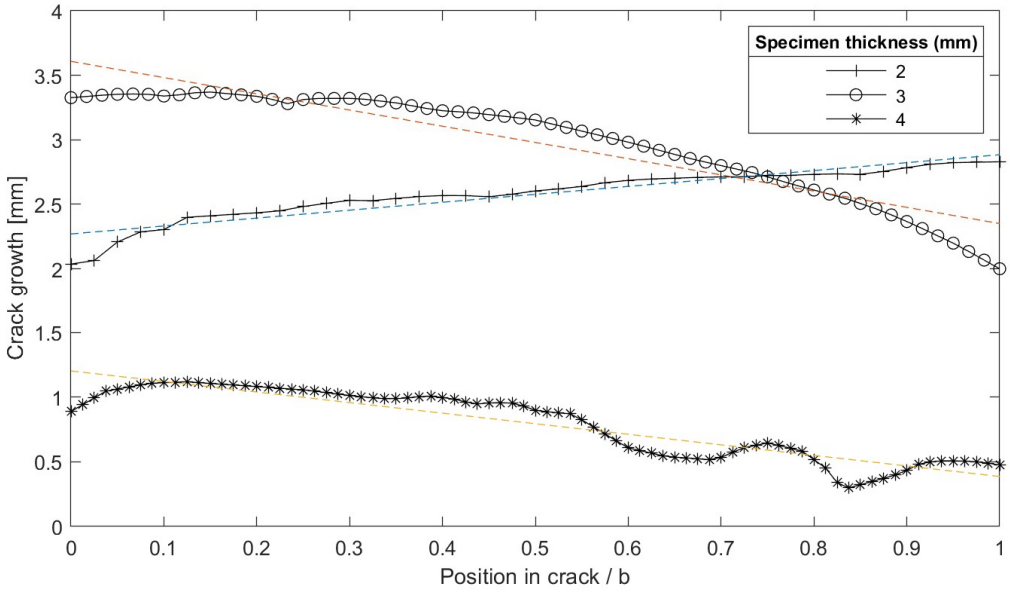

Figure 15. Normalized final fracture of thicknesses of 2, 3, and 4 mm.

3.6. Overload Crack Shape Analysis

A linear data trend of the crack shape upon overloading and final fracture was calculated. It was observed that the shape of the overload crack and the final fracture had an apparent geometric similarity. In Figure 16a, which corresponds to the 2-mm tubular specimen, the slope of the line due to overload was 0.50, while that corresponding to the final fracture was 0.61. The same previous analysis was carried out in Figure 16b, corresponding to the 4-mm-thick tubular specimen. For the 2-mm specimen, overload and fracture crack geometry are shown. The slopes of the lines associated with linear data fitting had a value of −0.816 for the overload and −1.23 for the final fracture. The specimens overloaded to mark the crack have different slopes on the straight lines due to data adjustment, a positive slope for the thickness of 2 mm, and a negative slope for the thickness of 4 mm. In flat specimens, in their central part, the slope due to data fitting has a value similar to zero [5].

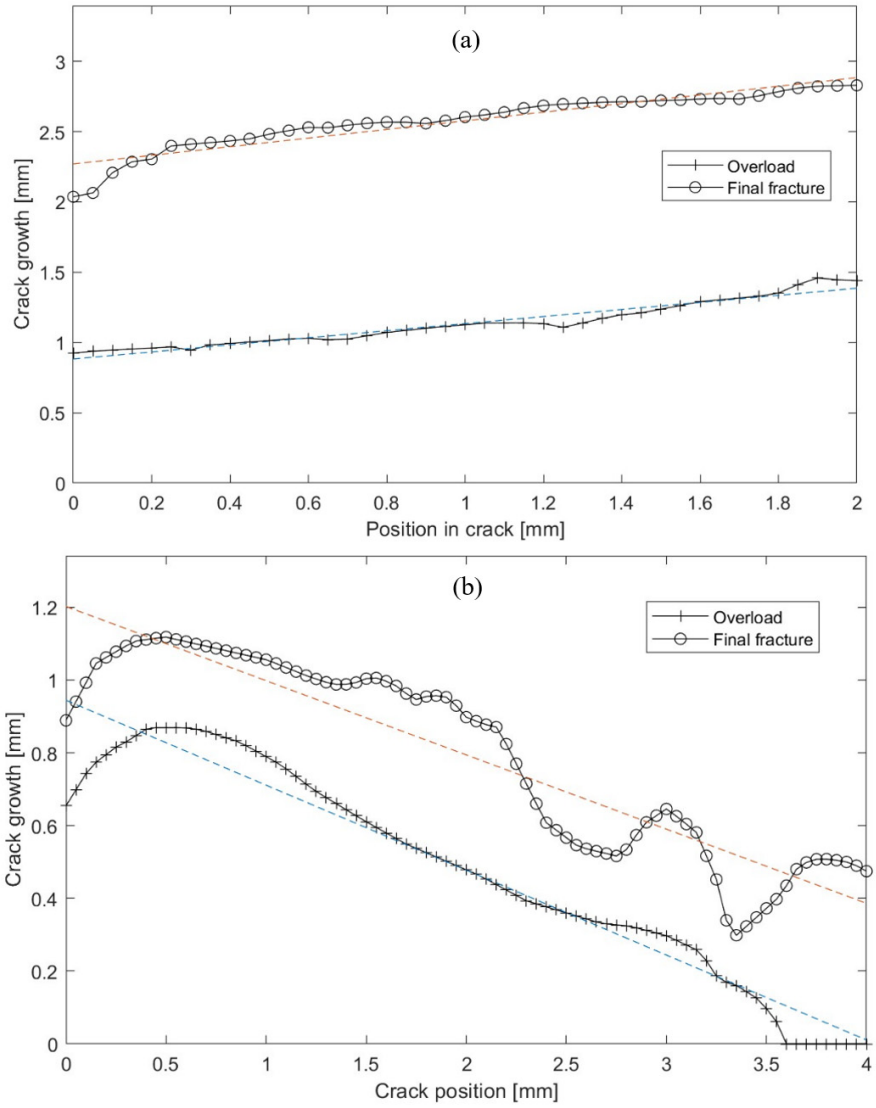

Figure 16. Crack shape with overload and final fracture. (**a**) 2 mm thickness; (**b**) 4 mm thickness.

4. Conclusions

An experimental analysis of the fracture zone and crack growth of tubular specimens subjected to cyclic loads in mode I was carried out, with a sinusoidal shape function and a frequency of 3 Hz. The analysis of results focuses on the variation of the stress intensity factor and in the crack geometries produced by fatigue until overloading and final fracture.

A quantitative graphic analysis of the presented phenomenon was carried out. These results led to the observation of characteristic behaviors in tubular specimens. Regarding the results, the following conclusions can be defined:

The parameter F_0 and the stress intensity factor increase their values proportionally to the growth of the crack. A marked difference was found in the values of the stress intensity factor on the external faces of the internal and external radii.

The maximum value of the stress intensity factor at which the specimens fail is associated with the internal radius for the specimen with a wall thickness of 2 mm and a value of 26.98 MPa $m^{1/2}$, while for the specimens with 3 and 4 mm of wall thickness, this occurs in the outer radius with values of 26.39 MPa $m^{1/2}$ and 24.76 MPa $m^{1/2}$, respectively. The three analyzed specimens exhaust their capacity to support loads when the stress intensity factor takes an average value of 26.04 MPa $m^{1/2}$, a different value from the static stress intensity factor due to crack growth.

In the tubular specimen with 3 mm thickness, four stages of crack growth were identified using artificial vision techniques. The crack was marked in the fatigue fracture zone in the tubular specimens with a wall thickness of 2 and 4 mm. For this, an overload was applied over 1500 cycles after starting the mechanical test by applying cyclic loads.

The geometry of the overburden crack was identified to be similar to that of the final fracture, when compared using a linear data trend, and its slopes were identified to change as the crack moved due to the application of cyclic loads. The difference in slopes was found with a value less than 0.44.

When evaluating the crack displacement of the tubular specimens, it was found that the crack propagation distance on the external faces of the specimen was different and was associated with the internal radii Ri and Re, a particularity that does not occur in the flat specimens, with similar crack displacement on their external faces. The area associated with the internal radius Ri and the external radius Re was calculated. A mean curved plane was defined for the calculation of the areas. A variation was identified in the calculated areas that are associated with Re and Ri. The variations related to the length of crack displacement and the calculated areas again highlight the differences with flat specimens.

The 2 mm thickness specimen followed its pattern with a more significant internal growth until breaking; we can consider it thin-walled.

The 4 mm thickness specimen presented in most of its development a tridimensional lenticular crack development, which would be the end of the very thick wall.

The sample with a wall thickness of 3 mm achieved behavior analogous to samples with two-dimensional cracks, but a transitory adaptation process occurred that is important to consider in order to correctly interpret the results obtained from the studies carried out with these tubular-type specimens.

The difficulty of evaluating the growth results of the crack on the outside alone is also shown. A numerical model approach is needed to improve the situation of the different stages detected.

The need to carefully analyze the mode I behavior of these specimens before addressing biaxial problems is highlighted.

Author Contributions: Methodology, L.A.-J., L.C., A.G.-H. and J.M.G.-M.; validation, A.G.-H. and J.M.G.-M.; formal analysis, L.A.-J.; investigation, L.A.-J., L.C., A.G.-H. and J.M.G.-M.; writing—original draft, L.A.-J.; writing—review and editing, L.A.-J., L.C., A.G.-H. and J.M.G.-M.; supervision, A.G.-H. and J.M.G.-M. All authors have read and agreed to the published version of the manuscript.

Funding: This research received no external funding.

Data Availability Statement: The original contributions presented in the study are included in the article, further inquiries can be directed to the corresponding author.

Acknowledgments: The authors would like to thank the Universidad de Malaga/CBUA and the University of the Armed Forces ESPE (Ecuador) for their contribution to this research.

Conflicts of Interest: The authors declare no conflicts of interest.

Nomenclature

a	Crack length
α	Crack displacement angle
b	Specimen thickness
K_I	Stress intensity factor
R	Crack radius
Ri	Internal radius of the tubular specimen
Re	External radius of the tubular specimen

References

1. De Jong, H.F. Effects of crack length and crack front geometry on KQ-values of aluminum 7075-t651 CT-specimens. *Eng. Fract. Mech.* **1981**, *14*, 539–547. [CrossRef]
2. Correia, J.A.F.O.; De Jesus, A.M.P.; Alves, A.S.F.; Lesiuk, G.; Tavares, P.J.S.; Moreira, P.M.G.P. Fatigue crack growth behaviour of the 6082-T6 aluminium using CT specimens with distinct notches. In *Procedia Structural Integrity*; Elsevier B.V.: Amsterdam, The Netherlands, 2016; pp. 3272–3279. [CrossRef]
3. *ASTM E647*; Method for Measurement of Fatigue Crack Growth Rates. ASTM—American Society for Testing and Materials: West Conshohocken, PA, USA, 1999; pp. 591–630.
4. Chen, C.J.; Su, M.N.; Wang, Y.H.; Deng, X.W. Experimental research on the fatigue crack growth behaviour of Q420C. *J. Constr. Steel Res.* **2022**, *192*, 107241. [CrossRef]
5. Bretschneider, E.; Lehmann, T.; Ihlemann, J. Experimental investigation of crack initiation and crack propagation in aluminum demonstrator specimens. *Mater. Today Proc.* **2022**, *62*, 2594–2598. [CrossRef]
6. Cai, L.; Li, W.; Hu, T.; Ji, B.; Zhang, Y.; Sakai, T.; Wang, P. In-situ experimental investigation and prediction of fatigue crack growth for aluminum alloys under single spike-overloads. *Eng. Fract. Mech.* **2022**, *260*, 108195. [CrossRef]
7. Vasco-Olmo, J.M.; Díaz, F.A.; Antunes, F.V.; James, M.N. Characterisation of fatigue crack growth using digital image correlation measurements of plastic CTOD. *Theor. Appl. Fract. Mech.* **2019**, *101*, 332–341. [CrossRef]
8. She, C.; Guo, W. Three-dimensional stress concentrations at elliptic holes in elastic isotropic plates subjected to tensile stress. *Int. J. Fatigue* **2007**, *29*, 330–335. [CrossRef]
9. Simandjuntak, S.; Alizadeh, H.; Smith, D.J.; Pavier, M.J. Three dimensional finite element prediction of crack closure and fatigue crack growth rate for a corner crack. *Int. J. Fatigue* **2006**, *28*, 335–345. [CrossRef]
10. Roychowdhury, S.; Dodds, R.H. A numerical investigation of 3-D small-scale yielding fatigue crack growth. *Eng. Fract. Mech.* **2003**, *70*, 2363–2383. [CrossRef]
11. Ellyin, F.; Wu, J. A numerical investigation on the effect of an overload on fatigue crack opening and closure behavior. *Fract. Eng. Mater. Struct.* **1999**, *22*, 835–847. [CrossRef]
12. Sehitoglu, H.; Gall, K.; Garcia, A.M. Recent advances in fatigue crack growth modeling. *Int. J. Fract.* **1996**, *80*, 165–192. [CrossRef]
13. Ferreira, S.E.; de Castro, J.T.P.; Meggiolaro, M.A.; de Oliveira Miranda, A.C. Crack closure effects on fatigue damage ahead of crack tips. *Int. J. Fatigue* **2019**, *125*, 187–198. [CrossRef]
14. Urrego, L.F.; García-Beltrán, O.; Arzola, N.; Araque, O. Mechanical Fracture of Aluminium Alloy (AA 2024-T4), Used in the Manufacture of a Bioproducts Plant. *Metals* **2023**, *13*, 1134. [CrossRef]
15. Vasco-Olmo, J.M.; Camacho-Reyes, A.; Gonzales, G.L.G.; Díaz, F. Investigation of Plasticity Effects on Growing Fatigue Cracks Using the CJP Model of Crack Tip Fields. *Materials* **2023**, *16*, 5744. [CrossRef] [PubMed]
16. Camas, D.; Garcia-Manrique, J.; Gonzalez-Herrera, A. Numerical study of the thickness transition in bi-dimensional specimen cracks. *Int. J. Fatigue* **2011**, *33*, 921–928. [CrossRef]
17. Tanaka, K.; Takahash, H.; Akiniwa, Y. Fatigue crack propagation from a hole in tubular specimens under axial and torsional loading. *Int. J. Fatigue* **2006**, *28*, 324–334. [CrossRef]
18. Shamsaei, N.; Gladskyi, M.; Panasovskyi, K.; Shukaev, S.; Fatemi, A. Multiaxial fatigue of titanium including step loading and load path alteration and sequence effects. *Int. J. Fatigue* **2010**, *32*, 1862–1874. [CrossRef]
19. Gladskyi, M.; Fatemi, A. Notched fatigue behavior including load sequence effects under axial and torsional loadings. *Int. J. Fatigue* **2013**, *55*, 43–53. [CrossRef]
20. Fatemi, A.; Gates, N.; Socie, D.F.; Phan, N. Fatigue crack growth behaviour of tubular aluminium specimens with a circular hole under axial and torsion loadings. *Eng. Fract. Mech.* **2014**, *123*, 137–147. [CrossRef]
21. Gladskyi, M.; Fatemi, A. Load sequence effects on fatigue crack growth in notched tubular specimens subjected to axial and torsion loadings. *Theor. Appl. Fract. Mech.* **2014**, *69*, 63–70. [CrossRef]
22. Mokhtarishirazabad, M.; Lopez-Crespo, P.; Moreno, B.; Lopez-Moreno, A.; Zanganeh, M. Optical and analytical investigation of overloads in biaxial fatigue cracks. *Int. J. Fatigue* **2017**, *100*, 583–590. [CrossRef]
23. Macek, W.; Pejkowski, Ł.; Branco, R.; Nejad, R.M.; Żak, K. Fatigue fracture surface metrology of thin-walled tubular austenitic steel specimens after asynchronous loadings. *Eng. Fail Anal.* **2022**, *138*, 106354. [CrossRef]
24. Macek, W.; Branco, R.; Szala, M.; Marciniak, Z.; Ulewicz, R.; Sczygiol, N.; Kardasz, P. Profile and areal surface parameters for fatigue fracture characterisation. *Materials* **2020**, *13*, 3691. [CrossRef] [PubMed]

25. Lv, W.; Ding, B.; Zhang, K.; Qin, T. High-Cycle Fatigue Crack Growth in T-Shaped Tubular Joints Based on Extended Finite Element Method. *Buildings* **2023**, *13*, 2722. [CrossRef]
26. Hu, C.; Xia, Q.; Zeng, E.; Zhu, J.; Yu, S.; Zhang, L.; Xu, F. Experimental and Numerical Investigation on Stress Concentration Factors of Offshore Steel Tubular Column-to-Steel Beam (STCSB) Connections. *Buildings* **2024**, *14*, 2004. [CrossRef]
27. Abatta-Jacome, L.; Lima-Rodriguez, A.; Gonzalez-Herrera, A.; Garcia-Manrique, J.M. Numerical Study of the Plastic Zone at the Crack Front in Cylindrical Aluminum Specimens Subjected to Tensile Loads. *Materials* **2023**, *16*, 6759. [CrossRef]
28. Sefene, E.M.; Tsai, Y.H.; Jamil, M.; Jatti, V.S.; Mishra, A.; AsmareTsegaw, A.; Costa, E.C. A multi-criterion optimization of mechanical properties and sustainability performance in friction stir welding of 6061-T6 AA. *Mater. Today Commun.* **2023**, *36*, 106838. [CrossRef]
29. Sanders, J.L. Circumferential through-Cracks in Cylindrical Shells under Tension. 1982. Available online: https://asmedigitalcollection.asme.org/appliedmechanics/article-abstract/49/1/103/388580/Circumferential-Through-Cracks-in-Cylindrical?redirectedFrom=fulltext (accessed on 15 January 2024).
30. Forman, R.G.; Hickman, J.C.; Shivakumar, V. Stress intensity factors for circumferential through cracks in hollow cylinders subjected to combined tension and bending loads. *Eng. Fract. Mech.* **1985**, *21*, 563–571. [CrossRef]
31. Maiti, S.K.; Savla, P.D. Experimental and finite element study on mode I stable crack growth in symmetrically stiffened compact tension specimen. *Eng. Fract. Mech.* **1993**, *44*, 721–733. [CrossRef]
32. Garcia-Manrique, J.; Camas, D.; Gonzalez-Herrera, A. Study of the stress intensity factor analysis through thickness: Methodological aspects. *Fatigue Fract. Eng. Mater. Struct.* **2017**, *40*, 1295–1308. [CrossRef]
33. Jin, H.J.; Wu, S.J. A new driving force parameter for fatigue growth of multiple cracks. *Int. J. Fatigue* **2017**, *96*, 10–16. [CrossRef]
34. Assias, S.L.G.; Kotik, H.G.; Ipiña, J.E.P. Fracture surface analysis of fracture mechanics specimens with splits: Determination of the physical crack extension. *Theor. Appl. Fract. Mech.* **2024**, *133*, 104509. [CrossRef]